regions while ignoring all buildings which block the lit regions, we define that the two VSs look at each other. In this procedure, the transmitter and the receiver are considered as VSs, and the lower bounds of all lit regions are then ignored. From the pairs of VSs, rays from the transmitter to the receiver are found by backward ray tracing in the plan view. The rays over buildings in the plan view account for forward rooftop diffractions. Since two sets of VSs are constructed, there may be duplicated rays, and so they must be removed.

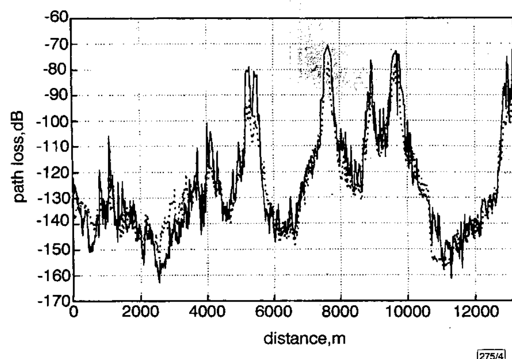

Fig. 4 *Comparison of predictions with measurements*

——— predictions
– – – – measurements

In the second step, for each ray in the plan view, the entire series of horizontal building edges lying between the transmitter and the receiver is available as the unfolded vertical profile of buildings. Using the vertical profile, the heights of the scattering points around buildings, as well as forward and backward rooftop diffraction points can be determined in a similar manner to that in [2], with the approximation that the rays diffracted at a horizontal edge are taken to lie in the plane of the vertical profile. This approximation introduces a small prediction error.

To determine the diffraction loss due to propagation over buildings, we first find significant edges which form the shortest path from the transmitter to the receiver and apply the UTD diffraction coefficients to those edges in a cascade. When applying the UTD, the edges in the transition region of a previous edge are excluded, and the accounted edges as well as the transmitter and the receiver are set to the 'UTD edge's'. Between each pair of 'UTD edge's' there can be additional edges that may interfere with the propagation field. Among those edges, the most significant edges up to 10 are accounted for by the method proposed by Whitteker [3] in the calculation of the additional loss. From one vertical profile, multiple rays which may undergo back diffractions from horizontal edges or ground reflections can be found, and they must be considered individually. Our method allows for a single back diffraction from a horizontal edge anywhere along the ray path. The Fresnel reflection coefficients and the UTD diffraction coefficients are then applied for the scatterings around the buildings.

For computational efficiency, we constructed two VSTs in the restricted areas around a transmitter and a receiver within radii R_T and R_R as shown in Fig. 2. This restriction causes a slight prediction error in most cases, and the radius must be larger as the source height is increased.

Results and conclusion: To check the accuracy of the proposed ray tracing method, prediction results are compared with measurements in Munich which have been supplied by the German GSM operator Mannesmann Mobilfunk GmbH. Fig. 3 shows the building layouts in the city as well as the transmitter location and measurement route. The measurements were carried out at 947MHz with the transmitter and receiver heights 13 and 1.5m above the ground, respectively. To predict the signal path loss, scatterings up to 3rd order including one diffraction were allowed in the areas within R_T = 500m and R_R = 200m, respectively. The sector averaged received power was calculated by summing the individual powers of the contributing rays [2]. The values of relative permittivity and conductivity were set at 4.44, 0.01S/m for buildings and 15, 7S/m for the ground.

Fig. 3 shows some dominant rays from the transmitter to one receiver in the measurement route. The detailed comparisons in the route are shown in Fig. 4. The average and standard deviation of the prediction error are 1.83 and 7.84dB, and so the predictions of the proposed method are in good agreement with the measurements.

© IEE 1999
29 March 1999
Electronics Letters Online No: 19990595
DOI: 10.1049/el:19990595

Hae-Won Son and Noh-Hoon Myung (*Department of Electrical Engineering, Korea Advanced Institute of Science and Technology, (KAIST), 373-1, Kusong-dong, Yusong-gu, Taejon, Korea*)

E-mail: hwson@cais.kaist.ac.kr

References

1 RIZK, K., WAGEN, J.F., and GARDIOL, F.: 'Two-dimensional ray tracing modeling for propagation prediction in microcellular environments', *IEEE Trans.*, 1997, **VT-46**, (2), pp. 508–518

2 LIANG, G., and BERTONI, H.L.: 'A new approach to 3-D ray tracing for propagation prediction in cities', *IEEE Trans.*, 1998, **AP-46**, (6), pp. 853–863

3 WHITTEKER, J.H.: 'Near-field ray calculation for multiple knife-edge diffraction', *Radio Sci.*, 1984, **19**, (4), pp. 975–986

AlGaN/GaN dual-gate modulation-doped field-effect transistors

C.-H. Chen, K. Krishnamurthy, S. Keller, G. Parish, M. Rodwell, U.K. Mishra and Y.-F. Wu

The first results concerning dual-gate AlGaN/GaN MODFETs are presented. The devices have 0.65μm gate lengths and were grown by metal organic chemical vapour deposition (MOCVD) on a sapphire substrate. The continuous wave (CW) output power is in excess of 2.5W/mm at 4GHz. The corresponding large-signal gain is 11.5dB and the power added efficiency is 30.6%. Dual-gate devices with different gate lengths can provide simultaneous high breakdown voltage and high current-gain cutoff frequency for the broadband power amplifiers.

2–20GHz phased array radars, now in development, require amplifiers operating over a decade bandwidth while providing tens to hundreds of Watts with high power added efficiency. GaN-based modulation-doped field-effect transistors (MODFETs) are attractive in high power applications due to a large breakdown voltage V_{br} ($P_{out} \leq V_{br}^2/8R_L$) [1 – 3]. 6W/mm power density at 10GHz has been demonstrated for devices on SiC substrate [3]. f_T > 60GHz has been achieved with a gate length L_g < 0.15μm [4]. In broadband commonsource power amplifiers, the gain bandwidth product is limited to $\sim f_T$. Decreasing L_g increases f_T, with the product $V_{br} f_T < E_{max} v_{sat}/\pi$, where E_{max} and v_{sat} represent the breakdown field and electron velocity [5]. Increased V_{br} is obtained at the expense of decreased f_T, and high power levels are obtained at the expense of reduced amplifier bandwidth.

A dual-gate device is electrically equivalent to a common-source (CS)/common-gate (CG) cascode pair [6], but occupies less die area. The current gain of the dual-gate device, $h_{21}(jf) = (f_{T1}/jf)(1 + jf/f_{T2})^{-1}$, deviates from that of the CS device $h_{21}(jf) = (f_{T1}/jf)$, only for $f > f_{T2}$, where f_{T1} and f_{T2} are the current gain cutoff frequencies of the CS and CG devices. To provide substantial current gain, f_{T1} must be several times the signal frequency f. In contrast, to avoid significant loss in h_{21} in the CG stage, it is sufficient to have an f_{T2} of 1.5–2f. The breakdown voltage is however determined by the CG device. Therefore, in a dual-gate device, it is advantageous to design the CS device with short L_g hence high f_T, and the CG device with long L_g hence lower f_T, but improved V_{br}. High bandwidth and high power are thus simultaneously obtained.

As a first demonstration, we fabricated dual-gate $Al_{0.25}Ga_{0.75}N$/GaN MODFETs with equal gate length (0.65μm) for CS and CG devices. Details of the epitaxial structure and fabrication process can be found in [1]. The sheet electron concentration and electron Hall mobility of as-grown modulation doped structures were ~1.72

× 10^{13}cm^{-2} and ~950cm^2/V s at room temperature. The gate of the CG device was connected to the source using MIM capacitors with 1000Å SiO_2 providing RF grounding. The first gate was separated by 0.7μm from the source and by 1.5μm from the second gate.

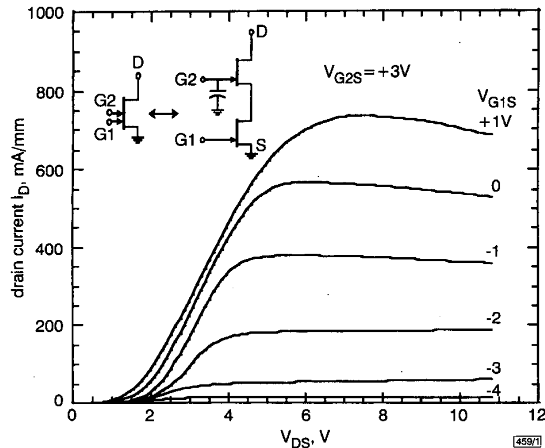

Fig. 1 *Drain output I-V characteristics of 0.65 × 150μm dual-gate AlGaN/GaN MODFETs, with second gate biased at +3V*

Maximum current > 700mA/mm

Fig. 1 shows the common source DC characteristics with the second gate biased at +3V. The pinch-off voltage is ~-4V and the gate-drain breakdown voltage is > 60V. Varying V_{G2S} varies V_{D1S}, hence the saturation current I_{DSS} and extrinsic transconductance g_m increase as V_{G2S} increases. The maximum transconductance g_m is ~205mS/mm.

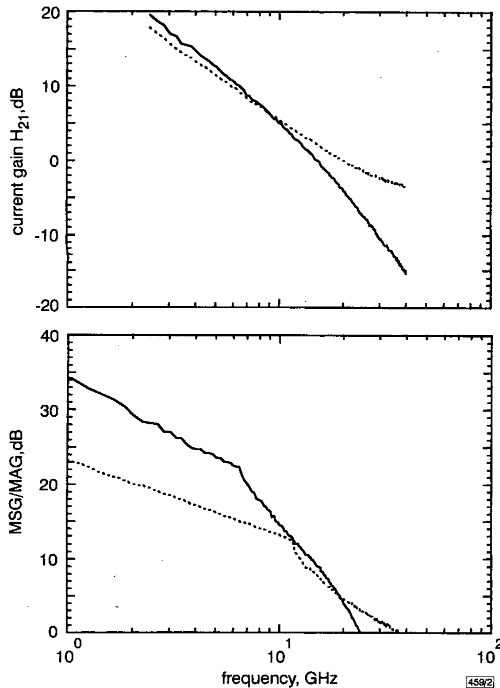

Fig. 2 *Gain-frequency characteristics of single-gate and dual-gate AlGaN/GaN MODFETs*

Drain biased conditions: +7V × 220mA/mm for single-gate device; +12V × 130mA/mm for dual-gate device

——— dual gate

- - - - single gate

DC to 40GHz device S-parameters were measured at a V_{DS} of +12V, and gate bias voltages of V_{G1S} = –2V and V_{G2S} = +3V, respectively. Both CS and CG FETs operate in the saturation region under this biasing condition. Fig. 2 shows a comparison of the h_{21} for single-gate and dual-gate MODFETs on the same wafer. The single-gate device exhibits $f_T \simeq$ 20.3GHz and $f_{max} \simeq$ 38.5GHz. The dual-gate device shows $h_{21}(jf) = (f_{T1}/jf)(1 + jf/f_{T2})^{-1}$, with f_{T1} = 22.2GHz and f_{T2} = 14.5GHz, and $f_{max} \simeq$ 24.2GHz. Owing to the reduced feedback signal (S_{12}) and increased output impedance (S_{22}) [6], the MSG/MAG of the dual-gate device is increased by 10dB for frequencies below 7GHz. Continuous wave (CW) microwave power measurements at 4GHz were performed on uncooled devices on sapphire substrate. The dual-gate device was biased at a source-drain voltage of +27.5V, and the second gate bias voltage V_{G2S} was +5.5V. The drain current at peak output power was 40mA (266mA/mm). The peak output power, as shown in Fig. 3, is 25.7dBm, corresponding to a 2.5W/mm power density. The small-signal linear gain, power added efficiency (PAE), and large-single gain are 17.6dB, 30.6%, and 11.5dB, respectively.

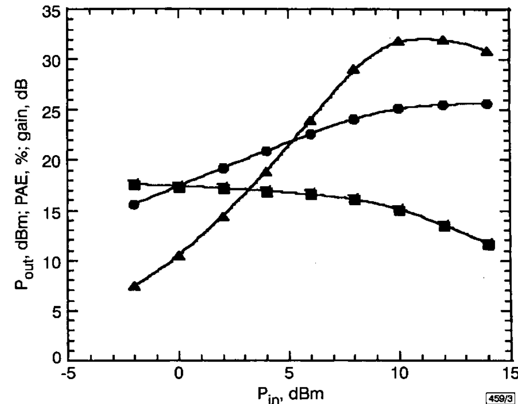

Fig. 3 *Microwave power performance of dual-gate device at 4 GHz*

Source-drain voltage was +27.5V, and second gate was biased at voltage V_{G2S} of +5.5V; small-signal linear gain is ~17.6dB, peak output power density is > 2.5W/mm, corresponding large-signal gain, and power added efficiency (PAE) are 11.5dB and 30.6%

▲ PAE

● P_{out}

■ gain

We have demonstrated the first dual-gate $Al_{0.25}Ga_{0.75}N$/GaN MODFETs. A CW output power in excess of 2.5W/mm was achieved at 4GHz, with power added efficiency > 30%. In the future, to obtain the desired characteristics of a high f_T (> 50GHz) while maintaining a large output power for broadband power amplifiers, the common-source device will be designed for a high f_T ($L_g \leq$ 0.15μm) hence low breakdown V_{br}, and the common-gate device can be designed for high V_{br} and consequently low f_T.

Acknowledgment: This work was supported by the Office of Naval Research contract number (N0014-98-1-0750) at the University of California, Santa Barbara.

© IEE 1999

12 April 1999

Electronics Letters Online No: 19990627

DOI: 10.1049/el:19990627

C.-H. Chen, K. Krishnamurthy, S. Keller, G. Parish, M. Rodwell and U.K. Mishra (*Department of Electrical and Computer Engineering, University of California, Santa Barabara, CA 93106, USA*)

Y.-F. Wu (*WiTech, 107 S. La Patera Lane, Goleta, CA 93117, USA*)

References

1 WU, Y.-F., KELLER, B.P., KELLER, S., NGUYEN, N.X., LE, M., NGUYEN, C., JENKINS, T.J., KEHIAS, L.T., DENBAARS, S.P., and MISHRA, U.K.: 'Short channel AlGaN/GaN MODFETs with 50-GHzf_T and 1.7W/mm output power at 10GHz', *IEEE Electron Device Lett.*, 1997, **18**, (9), pp. 438–440

2 PING, A.T., CHEN, Q., YANG, J.W., KHAN, M.A., and ADESIDA, I.: 'DC and microwave performance of high-current AlOaNIOaN heterostructure field effect transistors grown on p-type SiC substrates', *IEEE Electron Device Lett.*, 1998, **19**, (2), pp. 54–56

3 SHEPPARD, S.T., DOVERSPIKE, K., PRIBBLE, W.L., ALLEN, S.T., and PALMOUR, J.W.: 'High power microwave GaN/AlGaN HEMTs on silicon carbide'. 56th Device Research Conf. Dig., 1998
4 CHU, K.K., CHUMBES, E.M., GREEN, B.M., SHEALY, J.R., and EASTMAN, L.F.: Unpublished, 1998
5 JOHNSON, E.O.: 'Physical limitations on frequency and power parameters of transistors', *RCA Rev.*, 1965, pp. 163–177
6 ASAI, S., MURAI, F., and KODERA, H.: 'GaAs dual-gate Schottky-barrier FET's for microwave frequencies', *IEEE Trans.*, 1975, **ED-22**, (10), pp. 897–904

Mid-infrared intersubband electroluminescence in InAs/AlSb cascade structures

K. Ohtani and H. Ohno

Mid-infrared intersubband electroluminescence is reported in InAs single quantum wells embedded in InAs/AlSb quantum cascade structures. The observed emission energy is in good agreement with calculations based on the multiband k·p theory. The dominant polarisation of the emitted light is perpendicular to the quantum well layers.

Quantum cascade lasers (QCL) are high performance mid-infrared light sources based on intersubband optical transitions, first demonstrated using GaInAs/AlInAs quantum well (QW) structures [1, 2]. The wavelength range covered by GaInAs/AlInAs QCLS includes the atmospheric windows (3–5 and 8–13μm) important for gas sensing and environment monitoring applications. Recently, high power continuous-wave (CW) operation (5 and 8μm, 200mW/facet) has been achieved at 80K [3, 4].

Sb-based InAs/AlSb QCLs have a number of advantages over GaInAs/AlIAs QCLs. The InAs/AlSb heterostructure has a highly tunable intersubband transition energy due to the larger conduction band offset (~1.35eV) compared to that of the GaInAs/AlInAs systems (~ 0.5eV). Also, a recent theoretical appraisal of Sb-based intersubband lasers (5μm) [5, 6] showed that the threshold current density can be as low as 750A/cm² at 300K, almost a factor of four lower than the theoretical prediction for the 5μm GaInAs/AlInAs QCLs [6]. This is due to the small electron effective mass in the InAs QW, which reduces the optical phonon scattering rate believed to account for the high threshold current density in GaInAs/AlInAs QCLs, and at the same time increases the dipole matrix elements of the intersubband transition. Although intersubband electroluminescence in InAs QWs utilising interband tunnelling between InAs/GaSb has been realised recently [7], electroluminescence from InAs/AlSb structures has not yet been achieved. In this Letter, we report the first observation of mid-infrared intersubband electroluminescence in InAs single QWs embedded in InAs/AlSb quantum cascade structures.

The samples were grown by a solid source molecular beam epitaxy system equipped with a compound As cell and a cracking Sb cell on undoped InAs(100) substrates. After the growth of 700nm Si-doped (3×10^{17}cm^{-3}) *n*-type InAs as a bottom contact layer, 10 periods of injector and active layer structures were grown. The injector structure consisted of digitally graded InAs/AlSb superlattices in which the InAs layers were Si-doped to $n = 2 \times 10^{17}$cm^{-3}. The active layer consisted of an InAs/AlSb single QW which comprised a 10ML AlSb barrier, a 30ML InAs quantum well, and a 5ML AlSb barrier. An alternate structure which had a thinner InAs well (26ML) was also grown. After growth of the injector/active layer structures, 200 nm Si-doped (3×10^{17}cm^{-3}) InAs was grown as a top contact layer. All layers were grown at 420°C. During growth of injector and active layers, the InAs growth rate was reduced to 0.2ML/s and the As pressure was kept at a minimum to yield the group-V stability condition in order to prevent As incorporation into Sb-based layers. The AlSb layers displayed 1 × 3 RHEED patterns, and the InAs layers displayed 2 × 1 RHEED patterns with a V/III beam equivalence pressure ratio of 5.5 for InAs and AlSb growth.

The grown sample was then processed into a 200μm × 200μm mesa by wet-etching and photolithography. Non-alloyed Cr/Au ohmic contacts were deposited on both top and bottom contact layers. The sample edge was then polished to a 45° wedge for light emission and mounted onto a copper cold finger of a cryostat for cooling down to ~ 77K. The electroluminescence measurement was performed with a rapid scan FT-IR spectrometer (Bio-Rad FTS-60A) using a lock-in detection technique with a resolution of 4cm^{-1} [8]. A liquid-nitrogen cooled HgCdTe detector was used; a polariser was inserted in the optical path to verify the polarisation of the emission. Current pulses at 15kHz with a duty cycle of 50% were used for the electroluminescence measurements. Under a forward bias, electrons are injected from an injection region into the first excited state (E_2) of the InAs QW. The electrons at E_2 undergo intersubband transitions (radiative and nonradiative) and relax to the ground state (E_1) of the InAs QW. The relaxed electrons then tunnel to the collector through a thin AlSb barrier; the collector acts as an injector for the next QW. From the multiband k.p theory [9], the energy separation between E_1 and E_2 of the 30ML InAs quantum well sample is 228meV and that of the 26ML sample is 267meV.

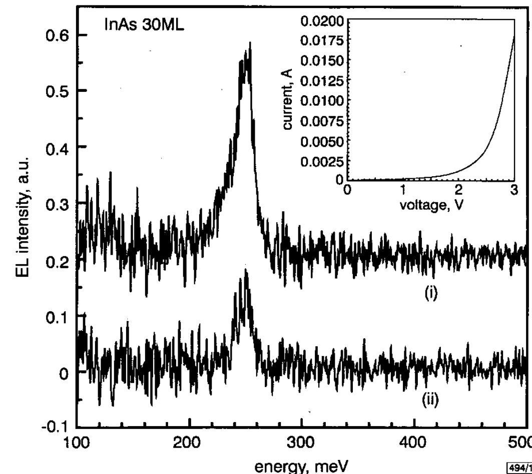

Fig. 1 *Electroluminescence spectra at ~77K for different injection currents*

(i) 80 mA
(ii) 50 mA
Inset: current-voltage characteristics at ~77K of intersubband cascade structure. Mesa area is 200μm × 200μm

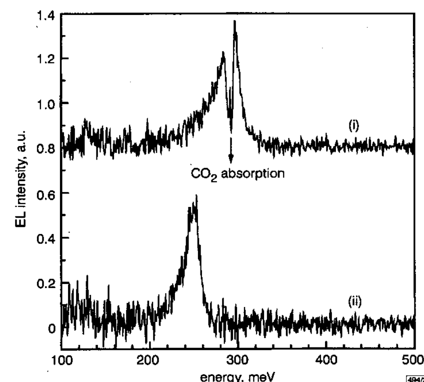

Fig. 2 *Electroluminescence spectra of intersubband cascade structures at ~77K for 80mA injection current density*

(i) 26 ML
(ii) 30 ML
Mesa area is the same for both samples

A typical current-voltage characteristic at ~77K is shown in the inset of Fig. 1. The injector blocks the current up to a bias of ~2.5V, after which the alignment of the injectors leads to current flow. Fig. 1 shows the electroluminescence spectra at ~77K under two different current bias conditions. An emission peak was observed at 247meV, corresponding to a wavelength of 5μm with full width at half maximum of ~18meV. The emission energy is in